Cavity quantum electrodynamic analysis of spasing in nanospherical dimers

Tharindu Warnakula,[1,*] Sarath D. Gunapala,[2] Mark I. Stockman,[3] and Malin Premaratne[1,†]

[1]*Advanced Computing and Simulation Laboratory (AXL), Department of Electrical and Computer Systems Engineering, Monash University, Clayton, Victoria 3800, Australia*

[2]*Jet Propulsion Laboratory, California Institute of Technology, Pasadena, California 91109, USA*

[3]*Department of Physics and Astronomy, Georgia State University, Atlanta, Georgia 30303 USA*

(Received 4 July 2019; revised manuscript received 19 August 2019; published 29 August 2019)

We present a detailed cavity quantum electrodynamic model of a nanospherical dimer and use it to analyze bright hybrid spasing modes there. Using an approximate numerical scheme, we model the complete spasing system as an open quantum system under the Lindblad dissipator formalism. We show that while in general the longitudinal dimer setups display higher intensity spasing as compared with transverse dimers, the latter actually consistently lead to output with higher coherence. Intriguingly, and somewhat counterintuitively, we find that transverse dimers only reach peak output at an intermediate dimer separation at which field confinement is not the strongest. We show that this is due to low radiative decay rates of transverse dimers with significant dimer gaps. We also find that transverse dimers outperform longitudinal dimers in terms of output intensity in a weakly pumped sparse gain medium made of dimers with relatively large separations. Moreover, in all the configurations considered, we find that the second-order coherence of the spasing output shows a peaked behavior just before the threshold, suggesting that the coherence is a useful indicator of spasing. Even though the scheme we describe is focused on dimers, owing to the generic form of the analysis presented, it can be easily extended to investigate spasing in the bright modes of multiple coupled plasmon sources.

DOI: 10.1103/PhysRevB.100.085439

I. INTRODUCTION

SPASER (surface plasmon amplification by stimulated emission of radiation) [1] is a device capable of generating extremely localized coherent plasmons at the nanoscale. Essentially describable as a nanoscale manifestation of the laser, such devices have been shown to have applications in ultramicroscopy [2], detection, and spectroscopy of biological and chemical agents [3], and various other biomedical applications including cancer therapy [4]. Operating at the nanoscale, a spaser can localize light, bypassing the diffraction limit when a conventional laser dimension becomes subwavelength. It achieves this by replacing the photons in a conventional laser by plasmons, a bosonic manifestation of the coherent electronic oscillations in materials (most often a noble metal like silver or gold) under electromagnetic fields. It replaces the feedback cavity of a laser with a nanoscale particle or structure capable of supporting the plasmon modes.

Since the pioneering model of spasers by Bergman and Stockman [5], there has been considerable interest in studying and fabricating realistic spasers due to incredible potential of the technology [4,6–8]. However, it was soon realized that mainly due to the high dissipation rates within plasmonic systems [9], the first simplistic models needed to be improved drastically.

In the past few years, hybrid nanostructures [10] that utilize electromagnetic field confinement and cooperativity effects have received significant attention as alternatives to the simple single nanoobject based spasers of the early days. Incredible advances have been made in terms of clever geometric arrangements that enhance the operation of spasers despite having to endure high intrinsic losses. The types of systems proposed can be roughly categorized into two domains: the devices operating utilizing the far-field interaction characteristics of plasmons and the devices operating utilizing the near-field interactions of plasmons placed next to each other. Of these, the former has shown immense promise in recent experimental successes that demonstrate ultranarrow linewidth lasing in periodically placed plasmon sources [11]. These effects have been theoretically predicted and explained [12,13]. However, due to the required spacing between plasmon sources, the sizes of these devices run well into the micrometer range. The second type of systems, that utilize the interaction of the near fields of plasmons, do not suffer from this size expansion. The first of these models was proposed in [14] where an interacting chain of spheres was analyzed using an electrodynamic formalism. The field enhancement and other desirable properties, including spasing, were predicted [15]. While these characterizations have been able to predict most of the behavior of nanosphere dimer based spasers, the analyses, however, have been limited to the classical and semiclassical domains and a fully quantum theory capable of handling such hybrid systems has been lacking until now. Quantum statistical effects play a key role within structures especially at the nanoscale, and the nature of these effects has not been studied in dimer setups. As a first step to filling

*tharindu.warnakula@monash.edu
†malin.premaratne@monash.edu

this void, we make a complete quantum characterization of a dimer based spaser also taking into account dissipation processes that heavily affect spasing output.

We perform our analysis using the standard dipole approximation. We also simplify our analysis by working within the quasistatic approximation, neglecting retardation effects. While dimers are simple as compared to the more complex spasing setups practically used nowadays, our technique can be extended to any hybrid setup supporting bright modes. We study the performance of a spaser made of a silver nanosphere dimer and also compare the spasing output to one composed of a single nanosphere. We only focus on the so-called bright plasmonic modes due to them being easily excitable using an external electric field. It has been shown that dipole modes in two isolated nanospheres hybridize when they are in close proximity, forming a dipole-active "bright" mode, and a dipole-inactive "dark" mode [16]. It is only the dipole active modes of the plasmons that can be coupled efficiently to and hence can be conveniently pumped by a linearly polarized electric field. We also analytically calculate both the couplings to individual gain medium chromophores in a three-dimensional (3D) gain distribution and the total radiative decays in the dimer system.

We perform our quantum analysis in the density matrix formalism. Such an approach is essential to account for intrinsic quantum effects in the setup. Even though, sometimes, computational cost is prohibitive in handling density matrix methods, some recent advances have enabled solving associated equations in polynomial time by exploiting their symmetry attributes [17]. Extension of Lamb's theory of lasing has also been successful in approximately solving the density matrix for coupled cavity-gain systems to high accuracy using the so-called reduced density matrix (RDM) approach [18]. With these tools, a new wave of advances and results regarding the behavior of spasing systems under quantum conditions have been obtained [17–20]. We utilize the RDM approach to solve the quantum density matrix in this work.

Our analysis can probe into some of the key characteristics of spasing systems composed of multiple nanoparticles placed next to each other. In particular, we study the full spasing curves, the plasmon probability distributions, as well as the second-order coherence of the generated surface plasmons to analyze the variation of spasing with dimer separation. We also analyze the effect of the gain medium distribution on the characteristics of dimer based spasers.

This paper is organized as follows: In Sec. II, we present the full theoretical model and the analytic derivations we use to model the spasing system. In Sec. III, we present the results derived through the equations of Sec. II and discuss the implications of the results for spasers and designers of spasers. We conclude our presentation by discussing possible future improvements and changes to the theoretical framework we present.

II. MODEL

In this section, we present the background details of the spasing model considered in this paper. We first explore the concept of plasmonic resonances of single metallic spheres (which we refer to as singlets). Then, we move onto the collective resonances of spherical dimers. We study the dimer systems as described by the coupled dipole approximation under the quasistatic limit, where one sphere's influence on the other can be simplified to be that of a point dipole placed at the origin of the first sphere. We study two configurations, longitudinal and transverse, of the dimer system based on the orientation of the external pumping field relative to the axis joining the spheres.

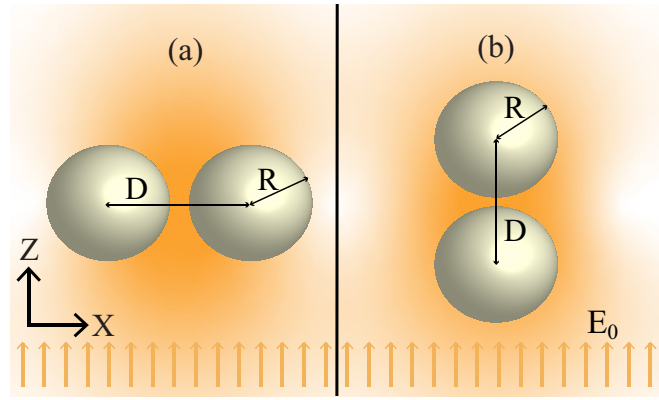

FIG. 1. The two dimer setups (a) transverse and (b) longitudinal. We orient the external electric field and hence the dipole moments along the z axis as shown. The y axis can be determined from the right-hand rule.

Next, we present the quantization procedure for both configurations and derive the quantized electric field operators and the associated coupling constants to external dipoles. We move onto calculating the radiative decay rates of the two setups afterward. While we treat the dimer modes and the decays of the dimer modes separately, we note there exist schemes such as the quasinormal mode (QNM) [21] approach and the generalized normal mode (GENOME) [22] approach that unify the treatment of the mode and the decays exactly through elegant utilization of complex mode frequencies and permittivities, respectively. Quantization of these modes gives us the quantum operators of the damped system along with the decays. On the other hand, our approach quantizes the free undamped mode and adds the dissipations self-consistently through Lindblad terms. While these two approaches yield similar results in the small dissipation limit, the method we use also has the advantage of simplicity and ease of analytical characterization and insight.

Finally, we model the two different spasing setups as open quantum systems consisting of plasmonic dimer systems coupled to a gain medium, that is immersed in an external environment. We use the Lindblad formalism to model the interactions between the quantum systems and external environment, enabling us to model both dissipation and decoherence.

Throughout this section, we will denote the center coordinate of the spheres by $\mathbf{r}_1$ and $\mathbf{r}_2$, and their separation along the axis joining the centers to be D. As shown in Fig. 1, the radii of the spheres will be taken to be equal to R and the relative permittivity of the metal will be denoted by ϵ_m. In this work, we mainly consider the metal to be silver and use the permittivities given by Jiang *et al.* [23]. These values are an improvement over the often-used Johnson and Christy

[24] measurements and have been derived under extremely controlled settings. We denote the relative permittivity of the medium in which the system is placed in by ϵ_b. In both the transverse and longitudinal setups, we will consider the external electric field to be oriented along the z direction. This forces the dipole moments in both setups to be oriented along the z direction. For the transverse setup, the two spheres will be placed along the x axis causing the electric field to be perpendicular to the axis joining the spheres. In the longitudinal setup, the spheres are arranged along the z direction and the electric field is parallel to the axis joining the spheres.

A. Plasmonic resonances in isolated metallic sphere

Metallic spheres are perhaps the most extensively studied structure as far as spasing is concerned. The structure of the surface charge distributions on metallic spheres in the presence of external fields and the nature of the plasmonic resonances that arise were known and explored for a long time [25]. The modes of induced surface charge distributions in metallic spheres can be shown to have the structure of spherical harmonics [26]. While these harmonics give rise to an infinite number of modes, the three lowest-order dipole modes corresponding to three orthogonal directions generally determine the dynamics and hence have been studied almost exclusively in the field of spasing [27]. While the higher-order multipoles have been shown to add significant effects to the spasing mode under certain conditions, we get away by not considering such modes by setting conditions just right for sustaining spasing in dominant dipole modes. In particular, we choose energy-level parameters as well as pumping parameters such that they will be completely decoupled from these multipoles. Due to the orthogonality of the charge distributions, we will also only be concerned with the charge distribution oscillations oriented along the z direction.

The dipole moment arising in a spherical metal nanoparticle in the presence of an external electric field $\mathbf{E}_0(t) = \mathrm{Re}\{\mathbf{E}_0 e^{-i\omega t}\}$ can be given as [28]

$$\mathbf{P} = \alpha R^3 \mathbf{E}_0, \tag{1}$$

where R is the radius of the sphere and the polarizability of the metallic sphere is given by $\alpha = \frac{\epsilon_m - \epsilon_b}{\epsilon_m + 2\epsilon_b}$. Note that we use the quasistatic approximation and, hence, the field is independent of the position vector $\mathbf{r}$ and the amplitude can be given by the constant vector $\mathbf{E}_0$. The resonance condition for such a nanosphere is determined by the real part of the denominator equaling to zero, $\mathrm{Re}\{\epsilon_m\} = -2\epsilon_b$. For a sphere placed inside a vacuum, this condition is the well-known resonance condition $\mathrm{Re}\{\epsilon_m\} = -2$. This dipole moment in turn induces an electric field outside the sphere given by

$$\mathbf{E}_{\mathrm{induced}} = \frac{[3(\mathbf{P}\cdot\mathbf{r})\mathbf{r} - |\mathbf{r}|^2\mathbf{P}]}{|\mathbf{r}|^5}. \tag{2}$$

B. Plasmonics resonances in metallic sphere dimers

Next, we turn to the problem of analyzing the resonances in metal sphere dimers. Using Eqs. (1) and (2), we can assign dipole moments to each of the two spheres and calculate the retarded electric fields at each sphere due to the other. Requiring the field values to be self-consistent gives us a solution for the dipole moments of each of the spheres. Subsequently, we use these dipole moment values to quantize the electric field in the dimer system. This approach only considers the dipole modes of the dimer system and neglects all other higher-order modes.

1. Plasmonic resonances in transverse dimers

We first present the quantization procedure for a silver nanosphere dimer with the dimer axis placed perpendicular to the direction of the external electric field [Fig. 1(a)]. We assume the size of the system to be much smaller compared to the wavelength of light and hence the complete system sees an external electric field value independent of position $\mathbf{r}$ given by $\mathbf{E}_0(t) = \mathrm{Re}\{E_0 e^{-i\omega t}\}\hat{\mathbf{z}}$, where E_0 is the constant amplitude of the electric filed in the z direction. We specifically choose this directionality of the external electric field to focus on the dipole moments and the plasmon oscillations along the z direction. The total electric field within the system can be written in the time harmonic approximation as $\mathbf{E}(\mathbf{r}, t) = \mathrm{Re}\{\mathbf{E}(\mathbf{r})e^{-i\omega t}\}$. The two spheres have identical polarizability values α, radii R, permittivities ϵ_m, separation D, and dipole moments in the z direction denoted by P_1 and P_2. Given E_1 and E_2 to be the electric field amplitudes in the z direction on the two spheres, for the electric field outside the two spheres we can write

$$\mathbf{E}(\mathbf{r}) = \mathbf{E}_0 + \alpha[E_1\mathbf{G}(\mathbf{r};\mathbf{r}_1) + E_2\mathbf{G}(\mathbf{r};\mathbf{r}_2)], \tag{3}$$

using the dyadic Green's function forms $\mathbf{G}(\mathbf{r};\mathbf{r}_d)$:

$$\mathbf{G}(\mathbf{r};\mathbf{r}_d) = \frac{R^3\{3[\hat{\mathbf{z}}\cdot(\mathbf{r}-\mathbf{r}_d)](\mathbf{r}-\mathbf{r}_d) - |\mathbf{r}-\mathbf{r}_d|^2\hat{\mathbf{z}}\}}{|\mathbf{r}-\mathbf{r}_d|^5}, \tag{4}$$

for $d = 1, 2$. The center coordinates of the spheres are given by $\mathbf{r}_1 = [-D/2, 0, 0]$ and $\mathbf{r}_2 = [D/2, 0, 0]$. At the exact locations of the spheres, Eq. (3) gives $E_1 = E_0 - \frac{P_2}{D^3}$ and $E_2 = E_0 - \frac{P_1}{D^3}$. Using $P_1 = \alpha R^3 E_1$ and $P_2 = \alpha R^3 E_2$, we can write two simultaneous linear equations for E_1 and E_2. Solving these would give us the exact values of the dipole moments to be

$$P_1 = P_2 = \frac{\alpha R^3 E_0}{1 + \frac{\alpha R^3}{D^3}}. \tag{5}$$

Comparing this equation to (1), this equation can be interpreted as a modification of the effective polarizability of the nanospheres to $\alpha_{\mathrm{eff}} = \frac{\alpha}{1+\frac{\alpha R^3}{D^3}}$. The electric fields inside the two spheres ($d = 1, 2$) can be given by [28]

$$E_{d,\mathrm{internal}} = E_d \frac{3\epsilon_b}{\epsilon_m + 2\epsilon_b} = E_d \alpha \frac{3}{\epsilon_m - \epsilon_b} \approx -\alpha E_d. \tag{6}$$

The last approximation is valid near resonance due to the fact that $\mathrm{Re}\{\epsilon_m\} \approx -2\epsilon_b$.

Next, we turn to the problem of quantizing the dimer electromagnetic field. Currently we have derived the electric field as generated by an external field. To derive the localized plasmon field, we need to find the localized solution of Maxwell's equations. To do this, following [29], we stimulate the system with an impulse of the form $\mathbf{E}_{\mathrm{impulse}} = E_0\delta(t)\hat{\mathbf{z}}$ instead of a constant external field. After $t = 0$, the response that remains

in the system will be exactly the localized solution

$$\mathbf{E}_{\text{dimer}}(\mathbf{r},\omega) = \frac{\alpha E_0}{1+\frac{\alpha R^3}{D^3}}[\mathbf{G}(\mathbf{r};\mathbf{r}_1)+\mathbf{G}(\mathbf{r};\mathbf{r}_2)]. \tag{7}$$

The Drude model for permittivities of silver, given the plasma frequency ω_p and decay rate γ_0 and the core permittivity ϵ_{core}, can be written as [1]

$$\epsilon_m = \epsilon_{\text{core}} - \frac{\omega_p^2}{\omega(\omega+i\gamma_0)}. \tag{8}$$

Assuming this model holds with $\epsilon_{\text{core}}=1$, and assuming that the external environment to be the vacuum ($\epsilon_b=1$), we can write the effective polarizability α_{eff} as

$$\begin{aligned}\alpha_{\text{eff}} &= \frac{\epsilon_m-\epsilon_b}{(\epsilon_m-\epsilon_b)\left(1+\frac{R^3}{D^3}\right)+3\epsilon_b} \\ &= \frac{\omega_F^2}{\omega_F^2\left(1+\frac{R^3}{D^3}\right)-(\omega^2+i\omega\gamma_0)}.\end{aligned} \tag{9}$$

Here, $\omega_F = \omega_p/\sqrt{2\epsilon_b+1} = \omega_p/\sqrt{3}$ is the Fröhlich frequency in the vacuum. Defining $\omega_0 = \sqrt{(1+\frac{R^3}{D^3})}\omega_F$ and making the standard approximation $\omega \sim \omega_F \sim \omega_0 \gg \gamma_0$, this allows us to rewrite Eq. (9) as

$$\alpha_{\text{eff}} \approx \frac{\omega_F/2}{(\omega_0-\omega)-i\gamma_0/2}.$$

Using this, we can rewrite Eq. (7) as

$$\mathbf{E}_{\text{dimer}}(\mathbf{r},\omega) = \frac{\omega_F E_0/2}{\omega_0-i\gamma_0/2-\omega}[\mathbf{G}(\mathbf{r};\mathbf{r}_1)+\mathbf{G}(\mathbf{r};\mathbf{r}_2)]. \tag{10}$$

This equation exactly predicts a resonant system with frequency ω_0 and damping $\gamma_0/2$. In the time domain this translates to

$$\mathbf{E}_{\text{dimer}}(\mathbf{r},t) = \frac{\omega_F E_0}{2}[\mathbf{G}(\mathbf{r};\mathbf{r}_1)+\mathbf{G}(\mathbf{r};\mathbf{r}_2)]\sin(\omega_0 t)e^{-\gamma_0 t/2}. \tag{11}$$

For a singlet nanosphere, the dipole resonance frequency is located at the Fröhlich frequency (ω_F). But for the bright mode of a transverse dimer, we see that the earlier analysis predicts a shifting of the resonance frequency. Furthermore, we see that this shift is exactly a blueshift. In the following analysis, we ignore decay rate and only reintroduce it later as part of the open quantum system model. We also note that while this result was derived with the assumption of $\epsilon_{\text{core}}=1$, for silver, this is not valid in general. The general expression only clutters the presentation with no added rigor, so we have opted for the simpler result. In particular, the general expression does not alter the form of the quantized field equation nor the calculated field intensities and coupling rate values.

As mentioned earlier, since we excite the system with a field in the z direction, we only consider the dipole mode oriented along the z direction. Since the dipole modes are orthogonally directed, such a procedure is justified and easily generalized to the case of a field in an arbitrary direction. Defining $\beta = \frac{\omega_F E_0}{2}$, the total energy W in this mode can be calculated as

$$W = \frac{\beta^2}{8\pi}\sin^2(\omega_0 t)\mathcal{W}(D), \tag{12}$$

where

$$\mathcal{W}(D) = \int |\mathbf{G}(\mathbf{r};\mathbf{r}_1)+\mathbf{G}(\mathbf{r};\mathbf{r}_1)|^2 \text{Re}\left\{\frac{d}{d\omega}(\omega\epsilon)\Big|_{\omega=\omega_0}\right\} d^3\mathbf{r}, \tag{13}$$

The extra derivative factor in the expression precisely accounts for the energy in dispersive media [30]. Note that this integration extends over infinite space. Defining normalization factor $N = \sqrt{\frac{8\pi\hbar\omega_0}{\mathcal{W}(D)}}$, and normalized amplitude $B = \frac{\beta}{N}$ enables us to write the total potential energy stored in the electric field as

$$W = \hbar\omega_0 B^2 \sin^2(\omega_0 t). \tag{14}$$

This expresses the potential energy of the electric field in a form reminiscent of electric field energy of an electromagnetic field. If we were quantizing a general electromagnetic field, the next step would be to compute the energy stored in the magnetic field and form the complete Hamiltonian. The magnetic and electric components of the electromagnetic field would then act as conjugate operator variables of a harmonic oscillator system. But in the near field of the dimer setup, the magnetic field is close to zero. A significant portion of the energy is actually stored in the kinetic motion of the electron cloud composing the plasmon [31]. However, estimating this proportion of energy stored outside of the electric field is not a trivial task. We handle this difficulty by considering the fact that, disregarding the dissipations, the total energy stored in the system should be constant and hence the energy stored in the electric field and the energy in the kinetic portions of the system including the current flows within each sphere must add up to a constant value [32]. For total energy to be conserved at all times t, the kinetic energy term must be of the form [29]

$$K = \hbar\omega_0 B^2 \cos^2(\omega_0 t). \tag{15}$$

This implies that our system is identical to a harmonic oscillator system with potential energy and kinetic energy being continually converted to each other in a periodic manner. Introducing the variable $A(t) = B\sin\omega_0 t$, the total Hamiltonian thus takes the form

$$H = \frac{\hbar}{\omega_0}(\omega_0{}^2 A^2 + \dot{A}^2). \tag{16}$$

This Hamiltonian takes the exact form of the quantum harmonic oscillator with conjugate variables A and $2\hbar A/\omega$. Making the identification $\hat{x}=A$ and $\hat{p}=2\hbar A/\omega$, we can transform to the position and momentum picture of the simple harmonic oscillator. $\hat{x}$ and $\hat{p}$ obey the usual commutation relation $[\hat{x},\hat{p}] = i\hbar$. Defining the bosonic annihilation operator as $\hat{a} = \hat{x} + \frac{i}{2\hbar}\hat{p}$, the Hamiltonian can finally be put in the form $H = \hbar\omega_0(\hat{a}^\dagger\hat{a}+\frac{1}{2})$. Using the newly defined creation and annihilation operators, we can cast the electric field in the form

$$\mathbf{E}_{\text{dimer}}(\mathbf{r}) = \tfrac{1}{2}N[\mathbf{G}(\mathbf{r};\mathbf{r}_1)+\mathbf{G}(\mathbf{r};\mathbf{r}_2)](\hat{a}^\dagger+\hat{a}). \tag{17}$$

Next we turn toward the question of the coupling between the dimer plasmon system and a dipole degree of freedom of a nearby chromophore. The interaction energy of a dipole interacting with an electric field $\hat{\mathbf{E}}$ can be given by $H_{\text{int}} = -\hat{\mathbf{P}} \cdot \hat{\mathbf{E}}$, where $\hat{\mathbf{P}}$ is the dipole moment operator of the chromophore. Assuming the dipole to originate from a two-level electronic transition, we could express the dipole moment operator as $\hat{\mathbf{P}} = \mu(\sigma_{10} + \sigma_{01})\hat{\mathbf{z}}$, where μ is the transition dipole moment and σ_{10}, σ_{01} are the raising and lowering operations for the electronic transition. Using (17) and applying the rotating-wave approximation to consider only the energy-conserving terms bring us to the final expression for the interaction Hamiltonian

$$H_{\text{int}}(\mathbf{r}) = \hbar g(\mathbf{r})(\sigma_{10}\hat{a} + \hat{a}^{\dagger}\sigma_{01}), \tag{18}$$

where the coupling constant $g(\mathbf{r})$ can be expressed as

$$g(\mathbf{r}) = -\tfrac{1}{2}\mu N[\mathbf{G}(\mathbf{r};\mathbf{r}_1) + \mathbf{G}(\mathbf{r};\mathbf{r}_1)]. \tag{19}$$

2. *Plasmonic resonances in longitudinal dimers*

Now, we turn to the question of longitudinal dimers. The equations and formulas applying to the longitudinal dimers remain approximately equal to the transverse. The main difference arises from the geometry of the setup, where, as dictated by Eq. (2), the electric fields at the position of the spheres can be expressed as $E_1 = E_0 + \frac{2P_2}{D^3}$ and $E_2 = E_0 + \frac{2P_1}{D^3}$. These equations give

$$P_1 = P_2 = \frac{\alpha R^3 E_0}{1 - 2\frac{\alpha R^3}{D^3}}. \tag{20}$$

The effective polarizability of the dimers gets modified to $\alpha_{\text{eff}} = \frac{\alpha}{1-2\frac{\alpha R^3}{D^3}}$. Using this form and following a similar procedure as we did in Eqs. (9) and (10), the electric field of the dimer system in the frequency domain can thus be obtained as

$$\mathbf{E}_{\text{dimer}}(\mathbf{r},\omega) = \frac{\omega_F E_0/2}{\omega_0 - i\gamma_0/2 - \omega}[\mathbf{G}(\mathbf{r};\mathbf{r}_1) + \mathbf{G}(\mathbf{r};\mathbf{r}_1)], \tag{21}$$

where $\omega_0 = \sqrt{1 - 2\frac{R^3}{D^3}}\omega_F$. Note that in the above equations, the $\mathbf{G}(\mathbf{r};\mathbf{r}_1)$ and $\mathbf{G}(\mathbf{r};\mathbf{r}_2)$ differ from that of the transverse setup by virtue of the difference in $\mathbf{r}_1$ and $\mathbf{r}_2$. For the longitudinal setup, $\mathbf{r}_1 = [0, 0, D/2]$ and $\mathbf{r}_2 = [0, 0, -D/2]$. The total energy in the electric field can be shown to have the same form as the transverse configuration given in Eq. (12), and after performing the quantization, we can derive the final form of the coupling constant $g(\mathbf{r})$ as

$$g(\mathbf{r}) = -\tfrac{1}{2}\mu N[\mathbf{G}(\mathbf{r};\mathbf{r}_1) + \mathbf{G}(\mathbf{r};\mathbf{r}_2)]. \tag{22}$$

C. Dissipation in plasmonic dimer setups

Next, we turn to the question of calculating the plasmon decay rate γ_{pl}. The decay is due to two main causes: the Ohmic dissipations within the metal γ_0, and the radiative dissipation caused by radiation into the far field γ_r. The Ohmic dissipation is a property of the metal and can be extracted from the permittivity of the metal. In this work, we use the dissipative rate as predicted by the Drude dielectric model [33] for silver. The radiative dissipations, on the other hand, depend on the electric fields in the system and hence need to calculated.

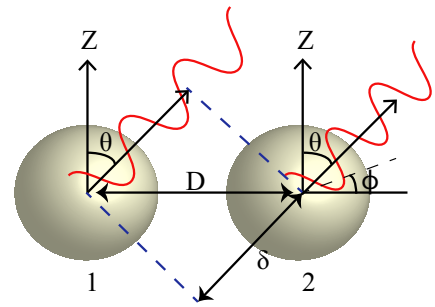

FIG. 2. The phase lag between the electromagnetic radiation emitted by the two sphere dipoles in a general polar angle direction θ and azimuthal angle ϕ.

We first focus on the singlet setup. The radiative decay rate can be calculated using the radial component of the Poynting vector in the far field. The time-averaged power radiated per unit solid angle per unit time can be given by [28]

$$\frac{d\langle W\rangle}{d\Omega} = \frac{c}{8\pi}k^4|\mathbf{P}|^2\sin^2(\theta). \tag{23}$$

This can be integrated to give the total power radiated per unit time to be $\frac{d\langle W\rangle}{dt} = \frac{ck^4}{3}|\mathbf{P}|^2$. Finally, the dissipation rate for a singlet can be calculated as $\gamma_r = \frac{1}{\langle W\rangle}\frac{d\langle W\rangle}{dt}$. $\langle W\rangle$ is the time-averaged power of the electrical field.

For a transverse dimer, the above derivation should be modified due to the existence of interference between the fields of the two spheres. To account for this, we consider the phase differences between the radiation waves emitted by the two spheres at a specific polar angle θ and azimuthal angle ϕ. As seen in Fig. 2, the radiation emitted in the direction (θ, ϕ) by sphere number 2 is exactly δ distance ahead of the radiation emitted by sphere 1, where δ is given by

$$\delta = D\,\sin(\theta)\cos(\phi). \tag{24}$$

This corresponds to a phase difference $\phi_{\text{tr}} = k\delta = \frac{2\pi D\sin(\theta)\cos(\phi)}{\lambda}$. Hence, the radiated electric field of sphere 2 in a certain radial direction with respect to sphere 1 can be written as $\mathbf{E}_2^{\text{rad}}(\theta,\phi) = \mathbf{E}_1^{\text{rad}}(\theta,\phi)e^{i\phi_{\text{tr}}}$. The total radiated electric field can thus be written

$$\mathbf{E}^{\text{rad}}(\theta,\phi) = \mathbf{E}_1^{\text{rad}}(\theta,\phi)(1 + e^{i\phi_{\text{tr}}}). \tag{25}$$

This radiation, in the far field, can be interpreted as emanating from a dipole placed at the position of dipole 1, but with a dipole moment scaled by the factor $(1 + e^{i\phi_{\text{tr}}})$. Using this interpretation, we can write the effective dipole moment in the direction (θ, ϕ) as

$$P^{\text{eff}}(\theta,\phi) = P(1 + e^{i\phi_{\text{tr}}}). \tag{26}$$

Going back to Eq. (23), the rate of radiative power dissipation per solid angle can be modified to

$$\frac{d\langle W\rangle}{d\Omega} = \frac{c}{8\pi}k^4|\mathbf{P}|^2\sin^2(\theta)|(1 + e^{i\phi_{\text{tr}}})|^2. \tag{27}$$

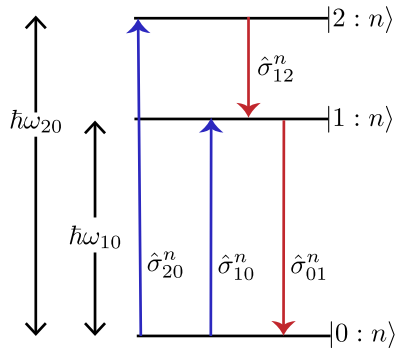

FIG. 3. The energy-level diagram for a single three-level gain medium chromophore is shown. The operators shown perform the transitions between the levels as indicated by the arrows.

Noting that $|1+e^{i\phi_{\rm tr}}|^2 = 4\cos^2(\frac{\phi_{\rm tr}}{2})$, we can write Eq. (27) as

$$\frac{d\langle W\rangle}{d\Omega} = \frac{c}{2\pi}k^4|\mathbf{P}|^2\sin^2(\theta)\cos^2\left(\frac{\pi D\sin(\theta)\cos(\phi)}{\lambda}\right). \quad (28)$$

Integrating this over all solid angles gives us the final value for the energy radiated per unit time. We can follow the exact same argument to calculate the radiative dissipation rate for the longitudinal setup. The phase difference turns out to be $kD\cos(\theta)$ and the expression for the energy radiated per unit solid angle per unit time is

$$\frac{d\langle W\rangle}{d\Omega} = \frac{c}{2\pi}k^4|\mathbf{P}|^2\sin^2(\theta)\cos^2\left(\frac{\pi D\cos(\theta)}{\lambda}\right). \quad (29)$$

D. Gain medium

We model the gain medium as a collection of three-level chromophores. This allows one of the electronic transitions to couple to the pumping field and the other transition to couple to the dimer plasmons, giving us control over the two transitions independently. The structure of the electronic levels is depicted in Fig. 3. The pumping electric field is coupled to the 0-2 transition while the 0-1 transition is coupled to the plasmons.

We assume that a rapid nonradiative decay takes place from level 2 to level 1. We also assume all the dipole moments of the chromophores to be aligned in the $\hat{\mathbf{z}}$ direction and the dipole transitions to be in resonance with the corresponding plasmons. For a chromophore indexed by n, we define the quantum state by a ket vector $|u:n\rangle$, with $u=0,1,2$, depending on the level. The transition operator from level v to u can then be defined as $\sigma^n_{uv} = |u:n\rangle\langle v:n|$. The 0-2 electronic transition has a dipole moment of 16 Debye and the 0-1 transition has moment 14.4 Debye in all results presented in this paper. We assign a nonradiative decay rate of 0.1 eV between levels 3 and 2, following similar theoretical analyses done on three-level spasing models [18]. We assume all other decay channels within the gain chromophores to be negligibly weak.

E. Quantum model

Now, we turn to modeling the complete spaser. A spaser consists of a gain medium transition coupled resonantly to a plasmonic mode. The plasmonic mode is furnished by the dimer setups while the gain medium transition is coupled to the 0-1 transition in our three-level gain chromophores. We start modeling of the system with the closed-system Dicke Hamiltonian [34] under the rotating-wave approximation

$$\begin{aligned}\hat{H} = {} & \hbar\omega_{\rm pl}\hat{a}^\dagger\hat{a} && \text{free Hamiltonian of plasmon mode}\\ & + \hbar\omega_{10}\sum_{n=1}^{N}\hat{\sigma}^n_{11} && \text{free Hamiltonian of level 1 electrons}\\ & + \hbar\omega_{20}\sum_{n=1}^{N}\hat{\sigma}^n_{22} && \text{free Hamiltonian of level 2 electrons}\\ & + P_{12}E_p\sum_{n=1}^{N}\left(e^{i\omega_{\rm pump}t}\hat{\sigma}^n_{01} + \text{H.c.}\right) && \text{pumping Hamiltonian}\\ & + \hbar g_n\left(\sigma^n_{10}\hat{a} + \hat{a}^\dagger\sigma^n_{01}\right) && \text{interaction Hamiltonian.}\end{aligned}$$

Here, $\omega_{\rm pl}$ is the plasmon resonance frequency and $\hat{a}^\dagger\hat{a}$ is the plasmon number operator. The second and third terms represent the total energy of the chromophores. The energy contribution of the nth chromophore is equal to $\hbar\omega_{20}$, $\hbar\omega_{10}$, or 0 depending on whether the chromophore is in state $|2:n\rangle$, $|1:n\rangle$, or $|0:n\rangle$, respectively. σ^n_{uv} indicates the transition operator from state v to u in the nth chromophore. The ω_{uv} indicates the energy gap between chromophore energy levels u and v. The fourth term represents the coherent pumping by an external electric field polarized in the z direction, with an amplitude E_p and at a frequency $\omega_{\rm pump}$. P_{12} is the dipole moment of the chromophore 2-1 transition. We consider both the pumping field and the dipole moments of the chromophores to be constant for all the chromophores. The final term in the Hamiltonian represents the interaction energy between the chromophore system and the plasmon mode where the g_n represents the coupling strength of the nth chromophore with the plasmon mode.

Using this Hamiltonian, we can derive the equation of motion for the density matrix of the quantum system as

$$\dot{\hat{\rho}} = \frac{1}{i\hbar}[\hat{H},\hat{\rho}]. \quad (30)$$

The model we have described above is also referred to as the closed Dicke model and it has been used to describe numerous cavity quantum electrodynamic systems. But, it does not take into account the various incoherent dissipations and decays a realistic system undergoes due to it being placed in an external environment. To account for these, we use the open Dicke model. In the open Dicke model, under the Born-Markov approximation, the equation of motion (30) is modified with the addition of the so-called Lindblad superoperators, which have nonunitary evolution characteristics. The superoperator is constructed using the quantum operators describing the incoherent dissipative transitions ($\hat{A}_d$) along with the average rates at which these occur (γ_d). In the interaction picture, the quantum density matrix evolution equation thus takes the

form [35]

$$\dot{\hat{\rho}} = \frac{1}{i\hbar}[\hat{H}, \hat{\rho}] + \sum_d D[\hat{A}_d]\hat{\rho}. \tag{31}$$

The superoperator can be generally represented as $D[\hat{A}_d]\rho = \frac{\gamma}{2}(2\hat{A}_d\rho\hat{A}_d^\dagger - \rho\hat{A}_d\hat{A}_d^\dagger - \hat{A}_d^\dagger\hat{A}_d\rho)$. Using different forms for $\hat{A}_d$ allows us to include considerations for processes such as plasmon decay ($\hat{A}_d = \hat{a}$) and decay of electrons of chromophores from level v to level u ($\hat{A}_d = \hat{\sigma}_{uv}^n$) in our model. Specifically, we model the decay of plasmons with $\hat{A}_1 = \hat{a}$, and the fast nonradiative decay of electrons from level 2 to 1 with $\hat{A}_2 = \hat{\sigma}_{12}^n$.

Solving these equations gives us access to the full density matrix that contains the complete information of the system. To consider how to solve this system of equations, let us first consider the size of a wave vector that describes the system. Assuming the plasmon modes may be truncated at a highest possible occupation number value of M, there are $M+1$ different possible values of the plasmon occupation number. For N chromophores each with three energy levels, there are 3^N possible configurations. This implies that a wave vector describing the system will have a size equal to $3^N(M+1)$. The density matrix in turn will have dimensions $6^N(M+1)^2$. This is a computationally impossible bound to handle and solve exactly. In recent years, much progress has been made toward solving equations of this form efficiently [19]. As presented in [17], if the assumptions of identical chromophores and incoherent pumping of chromophores are valid, the problem could be cast into a problem of size $O(N^4M)$ and numerically exactly solved. But, in many realistic setups, these assumptions may be too restrictive. Another practically useful and faster method of approximately solving the system involves using the reduced density matrix (RDM) approach [20]. It obtains a closed set of equations for the steady-state density matrix of the system using reasonable approximations. The main equation solved is the reduced density matrix for plasmon number states $\rho_{\mu,\nu}$, in terms of coupled individual chromophore density matrices $\rho_{u\mu,v\nu}^n$, where n identifies the particular chromophore and $u, v = 0, 1, 2$ denote the energy level of the electron of that chromophore:

$$\begin{aligned}\frac{\partial}{\partial t}\rho_{\mu\nu} = &-i(\mu-\nu)\omega_{\rm pl}\rho_{\mu\nu} - \gamma_{\rm pl}\frac{\mu+\nu}{2}\rho_{\mu\nu} \\ &+ \gamma_{\rm pl}\sqrt{(\mu+1)(\nu+1)}\rho_{\mu+1\nu+1} \\ &- \sum_{n=1}^{N} ig_n\left(\sqrt{\mu}\rho_{1\mu-1,0\nu}^n - \sqrt{\nu}\rho_{0\mu,1\nu-1}^n\right) \\ &+ \sum_{n=1}^{N} ig_n\left(\sqrt{\nu+1}\rho_{1\mu,0\nu+1}^n - \sqrt{\mu+1}\rho_{0\mu+1,1\nu}^n\right).\end{aligned} \tag{32}$$

This method has shown to provide approximately useful values for the density matrix equations for a three-level gain medium in a wide range of parameters with just $O(NM)$ time complexity [18]. In this work, we use the RDM approach due to the convenience and also its ability to handle heterogeneous gain media. We refer the reader to [18] for a complete treatment on the method and the associated derivation of equations.

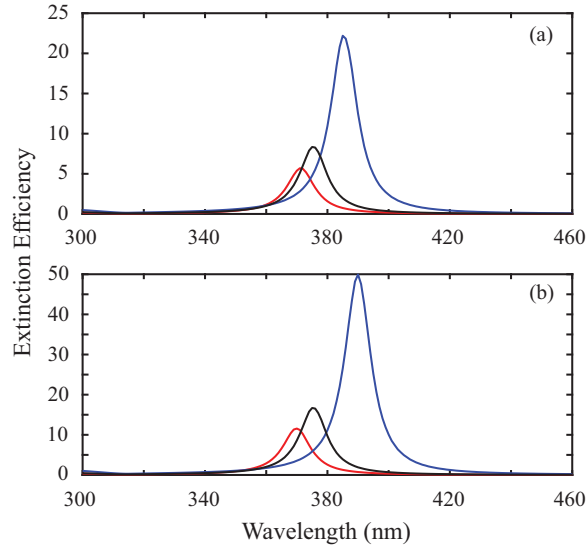

FIG. 4. The extinction efficiencies for 10-nm singlet (black), transverse dimer (red), and longitudinal dimer (blue) setups for two dimer separations. (a) $D = 25$ nm; (b) $D = 30$ nm.

III. RESULTS AND DISCUSSION

Here, we present our results on the various important quantities and factors affecting spasing in the dimer setup. For all the simulations presented henceforth, we assume $\epsilon_b = 1$. This is realistic for a sufficiently sparse distribution of solid chromophores around the plasmonic medium. In cases where this assumption may not be valid, the Maxwell-Garnett formula [36] should be used to calculate the effective value of the permittivity of the external environment.

A. Extinction cross sections and resonance frequency

First, we turn to the extinction profiles of the spasing setups to extract the resonance frequencies. The extinction efficiency for dimer setups can be given by [37]

$$C_{\rm ext} = \frac{4\pi k}{S_d E_0^2}\sum_i {\rm Im}\{\mathbf{E}_0.\mathbf{P}_i\}. \tag{33}$$

Here, the cross-sectional area $S_d = \pi R^2 + 2RD$ for transverse dimers and $S_d = \pi R^2$ for longitudinal dimers. The sum runs over the two dipoles. We note here that since our formulation only considers the near field, the extinction cross sections presented are equivalent to absorption cross sections. Figure 4 plots the extinction cross sections for singlet, transverse dimer, and longitudinal dimer configurations for 10-nm silver spheres at a dimer gap of $D = 25$ and 30 nm. As expected, the resonance peak redshifts for transverse dimers and blueshifts for longitudinal dimers at larger separation values. The efficiencies also slightly decrease at larger separation. As far as the linewidths are concerned, all dimer setups have similar or comparable linewidth as calculated as a FWHM value of $\approx$11 nm. This is as predicted by Eqs. (10) and (21), where we see that the linewidth for both dimer setups are equal to the singlet linewidth $\gamma_0/2$.

The transverse dimer bright mode, being an antibonding mode, experiences a blueshift while the longitudinal dimer

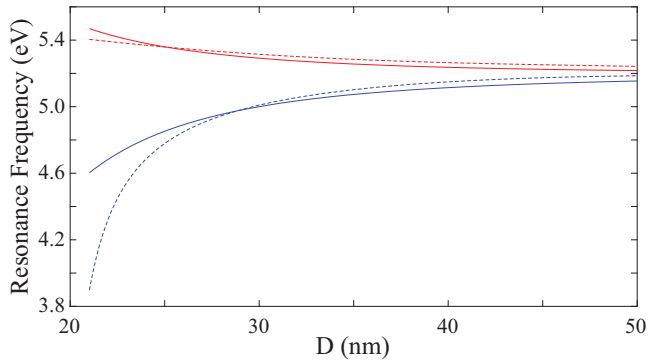

FIG. 5. The predicted resonance frequencies for 10-nm transverse dimer (red) and longitudinal dimer (blue) configurations by the formula we derive (solid lines) and the predictions of the full multipole theory (dashed lines).

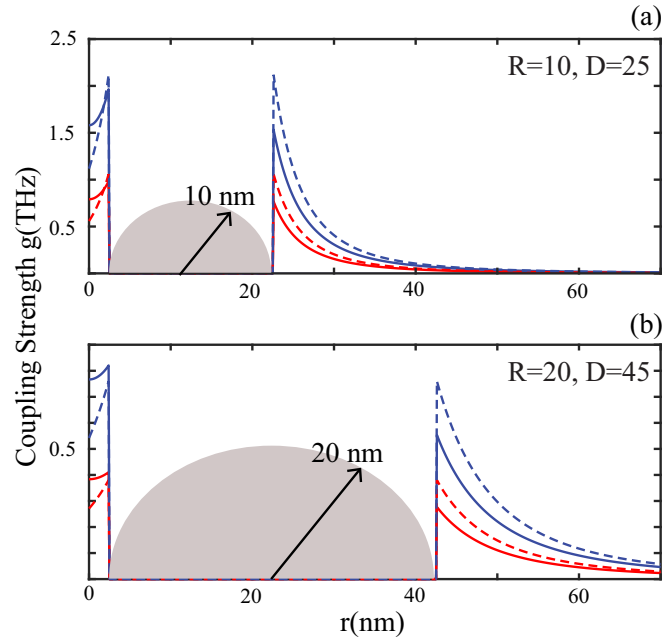

FIG. 6. Coupling strengths for a chromophore with 1 Debye moment along the z axis, placed at different distances from singlet and dimer plasmon setups. Solid lines plot the two dimer setups, transverse (red) and longitudinal (blue) with the chromophore placed on the dimer axis. The dashed lines represent the singlet with the chromophore placed along the metal nanoparticle dipole moment (blue) and placed perpendicular to the dipole moment (red).

experiences a redshift on account of its bright mode being a bonding mode. The equations we derived for the resonance frequency during the quantization of the dimer systems also predict a similar pattern. To study the accuracy of these formulas derived in the dipole approximation, in Fig. 5 we plot the resonance frequencies as predicted by the formulas $\omega_0 = \sqrt{1 - 2\frac{\alpha R^3}{D^3}}\omega_F$ for the longitudinal dimer and $\omega_0 = \sqrt{1 + \frac{\alpha R^3}{D^3}}\omega_F$ for the transverse, with those as predicted by the full multipole calculations of plasmon hybridization theory [38]. The multipole predictions are derived assuming a Drude model with plasma frequency $\omega_p = 9$ eV for 10-nm silver spheres. We observe that the formulas do in fact predict the resonance frequencies reasonably well for separations $D >$ 25 nm. At shorter distances, the effects of multipoles and other electron cloud distortion based effects play a significant role. Transverse and longitudinal dimers actually experience asymmetric shifting of the resonance frequency due to the presence of the factor of 2 in the formula for the longitudinal resonance frequency. Considering differently polarized external electric fields will allow the extraction of similar resonance frequency shifts for the dark modes within the dipole approximation as well.

From here on, we use the frequencies at the resonance peaks in the extinction spectra as the resonance frequencies of the various dimer setups. We do this to base our calculations on experimentally verified values rather than the formula we have derived which carries the intrinsic inaccuracies of the Drude model. We have verified through separate calculations that these peaks do indeed correspond to the zeros of the real part of the denominator of the effective polarizability α_{eff}.

B. Coupling strength

The coupling strength, as given by Eqs. (19) and (22), between the plasmon setup and the gain medium dictates much of the characteristics of spasing including the threshold. Next, we investigate the strength of the coupling between the dimer setups and a gain chromophore placed at different locations. We also study the coupling strength between a singlet nanosphere and a chromophore placed at different locations. The separate configurations we study are elucidated in the inset of Fig. 7.

All these quantities are plotted in Fig. 6 for silver spheres of radii 10 and 20 nm and separation values $D = 25$ and 45 nm, respectively. As can be seen, when the spheres in a dimer are close enough (low D values), the field confinement in-between the two spheres is great enough to support coupling strengths exceeding the singlet setup. We also observe that the larger spherical nanoparticles support the greater enhancement of the coupling relative to the singlet setup while the smaller nanoparticles have higher absolute values of the coupling strength. Figure 6 also indicates that the longitudinal dimer setup has the better coupling characteristics and has the potential to form the basis for better spasing setups.

Next we study the impact of the separation D on the coupling. Figure 7 plots the variation of the coupling strength of a chromophore of moment 1 Debye placed at the midpoint of a dimer setup consisting of metal nanospheres of radius $R =$ 10 nm. As can be seen, the longitudinal setup again has greater coupling strength at the mid-point as compared to the transverse setup. For reference, we have also included the coupling constants for a chromophore placed at the same distance away from a singlet setup. As we discovered earlier, the longitudinal chromophore placement in the singlet configuration performs much better as compared to the transverse placement, but not as well as the longitudinal dimer configuration. This again demonstrates the benefits of the dimer setup as compared to the singlet as far as spasing is concerned.

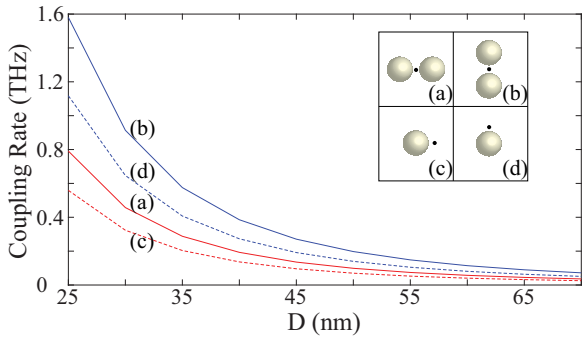

FIG. 7. The coupling strength (g) of the dimer longitudinal and transverse setup to a chromophore placed at the midpoint of the dimer axis (solid lines) for various dimer separation values (D). The radius of the nanospheres are set at $R = 10$ nm. The singleton coupling strengths for chromophores placed at the same distance are shown by the dashed lines. The inset depicts the placement of the gain chromophore (black circle) in each case.

C. Radiative damping rate

Next, we turn our attention toward modeling the total dissipations within the dimer systems. We model Ohmic losses γ_0, using the Drude dissipation parameter. We use the experimental data for silver from [23] and perform a curve fitting to obtain the value of γ_0. We obtain $\gamma_0 = 47.1$ meV $\sim$ 11.1 THz. Since the Ohmic losses in the system for silver are constant between different configurations, we only study the change of the radiative dissipation component γ_r.

Using Eqs. (12), (28), and (29) we can present the radiative dissipation rate for dimer setups with resonance wavelength λ as

$$\gamma_r = \frac{32\pi^4 cR^6}{\mathcal{W}(D)} \frac{\mathcal{I}(D/\lambda)}{\lambda^4}, \tag{34}$$

where $\mathcal{I}(D/\lambda) = \iint 4\,\sin^3(\theta)\cos^2(\frac{\pi D\sin(\theta)\cos(\phi)}{\lambda})d\theta\,d\phi$ for transverse configurations and $\mathcal{I}(D/\lambda) = \iint 4\,\sin^3(\theta)\cos^2(\frac{\pi D\cos(\theta)}{\lambda})d\theta\,d\phi$ for longitudinal configurations with $\mathcal{W}(D)$ given by Eq. (13). The $\mathcal{I}$ terms can be associated with the effects of interference between the two dipoles and $\mathcal{W}$ term is proportional to the total average power of the dimer system. We plot $\mathcal{W}$ against dimer separation for 10-nm dimer setups in Fig. 8(b). As can be seen, the proportional changes in power is extremely small and hence can be considered negligible. To understand why this is justified, consider the electrical energy of an isolated sphere W_s. For spheres placed close by in transverse configuration, the interaction energy $W_I \propto W_s R^3/D^3$ [28]. Hence, the proportional change in $\mathcal{W}(D)$ between two spheres placed at infinity and spheres placed at distance D can be given by $\Delta\mathcal{W} = R^3/2D^3$. As we saw earlier the proportional change in λ^{-4}, $\Delta\lambda^{-4} = (1 + R^3/D^3)^2 - 1$. Since $2R^3/D^3 + R^6/D^6 \gg R^3/2D^3$, we conclude that the change in $\mathcal{W}(D)$ is negligible. A similar argument can be followed for the longitudinal case. The key factors governing the dissipation rate hence are the interference $\mathcal{I}$ and the resonance wavelength λ.

We plot the change in radiative dissipation rate for transverse and longitudinal dimers with dimer separation in Fig. 8(a). We first notice that the radiative dissipation rates

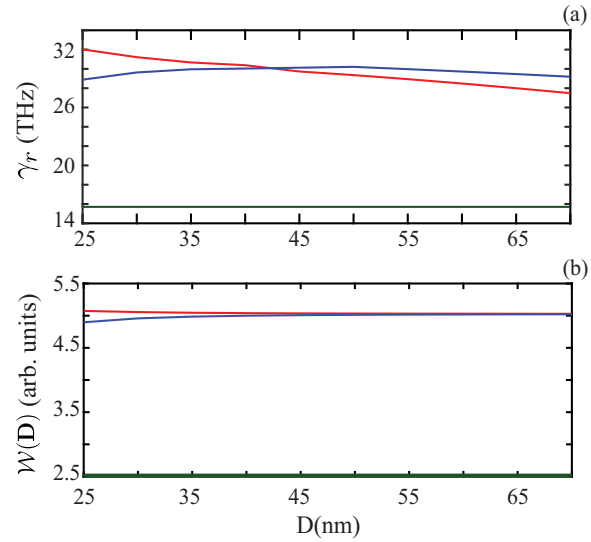

FIG. 8. The radiative dissipation rates (a) and mean power (b) for transverse (red) and longitudinal (blue) dimer setups composed on nanospheres of radius 10 nm at various dimer separations. In both graphs, the solid green line indicates the level for a singlet with the same radius.

for the sizes of nanospheres we consider dominate the Ohmic losses. At the smallest dimer gap we study (5 nm), the transverse dimer shows higher radiative dissipation as compared to the longitudinal.

However, more interestingly, the interference and resonance frequency shifts manifest interesting properties as spacing between the nanospheres is increased. In general, the transverse setups display a steady decline for the range of spacings we study. The longitudinal setup on the other hand goes through a maximum and starts declining. As can be seen in the figure, in the extremely close configurations (small D), the transverse dimer radiates energy at a higher rate as compared to the longitudinal dimer. But, at a certain separation, the transverse setup dips steeply below the longitudinal curve and continues downward. This implies the reduction of the transverse dimer radiative dissipation at larger separations. This can be understood in terms of the two key terms in Eq. (34). The $\mathcal{I}(D/\lambda)$ term diminishes for larger values of D while the λ^{-4} term also diminishes due to the redshift of the resonance frequency for larger separations. These two effects combine to account for the reduction in transverse dimer dissipation rate.

For the longitudinal dimer, while $\mathcal{I}(D/\lambda)$ diminishes for larger separations, the resonance frequency experiences a blueshift, causing the λ^{-4} term to actually dominate for smaller separations causing the peaked behavior we observe. For larger separations, however, the interference term dominates causing reduction of dissipation. Hence, heuristically, we can say that the radiation interference and resonance frequency shifts cooperatively cause reduction in radiative dissipation in transverse dimers, while for longitudinal dimers, those two effects act in opposition resulting in a peaked behavior for intermediate dimer separations before interference dominates to bring down total dissipations.

We note that a similar analysis was performed in [39], but the interference effects were neglected resulting in a radiative dissipation that only depended on hybridized resonance wavelength λ. Reference [40] also performs a similar analysis by calculating the linewidth of scattered spectra of dimers. The results there agree with our predictions qualitatively but the analysis therein is performed approximately which results in a prediction of λ^{-2} dependence of the radiative dissipation. We attribute this discrepancy to the fact that only the kinetic energy of oscillating charges were considered in [40], whereas detailed energy balance in plasmonic systems requires the consideration electrical energy = kinetic energy + magnetic energy [31].

D. Spasing characteristics

Next, we approach the question of modeling the action of a spaser, the plasmonic component of which is formed by a dimer setup composed of 10-nm radius silver nanospheres. As previous results demonstrated, the main characteristics of a dimer setup is the the higher coupling rate to gain chromophores in the dimer gap and the higher radiative dissipations. We present results that demonstrate the effects of these two key differences between the two dimer configurations as well as between the dimer setups and the singlet setup.

Nonlinear quantum effects come into play when the dimer gap is extremely small due to to the quantum nature of the electrons, nonlocal screening effects, and tunneling of electrons [41]. In addition to that, as we observed earlier in the hybridized resonance frequency calculations, the dipole approximation fails to account for the resonance frequency shifts in a dimer for extremely small separations. Hence, in all our simulations, we maintain a gap $(D - 2R)$ of at least 5 nm between the metal spheres. At this separation level, it has been shown that the bright mode of the dimer is sufficiently separated from other higher-order modes [42,43] except for the corresponding dark mode. However, due to the symmetry of the excitation source (plane wave) and the gain medium, we can neglect the antisymmetric dark mode excitation. Due to these reasons, in what follows, we model the dimer as a single-mode spasing system operating in the bright mode.

The main setup we use for the simulation and characterization of the spasing properties is shown in the inset of Fig. 9 as an example for the transverse spasing setup. We study the singlet setup, transverse dimer setup, and the longitudinal dimer setup, each of which is surrounded by a cuboid-shaped discrete gain medium distribution and we maintain a gain chromophore number density of 0.125 cm^{-3}. For gain chromophores with molecular sizes spanning the angstrom range, this value is realistic and it also allows us to make the sparsity assumption for the gain medium. We take the lengths of the gain medium extent in the three directions to be L_x, L_y, and L_z with the chromophores stationed at the grid points. Note that the gain medium cuboid is always centered at the midpoint of the dimer axis. We assume that the chromophore 0-1 transition is exactly in resonance with the plasmons in each of our simulations with the second electronic level lying a further 0.1 eV higher from level 1 of the chromophores. This value allows the 1-2 electronic transition to be decoupled from the higher-order multipoles for the plasmons we consider and also is commensurate with values used in similar theoretical investigations done on three-level spasing models [18].

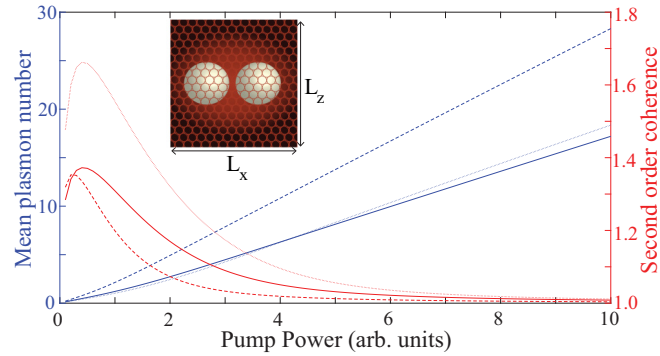

FIG. 9. The mean plasmon numbers (blue) and the second-order coherence values (red) for dimer and singlet configurations consisting of 10-nm nanospheres. The transverse dimer curves are denoted by the solid lines, the longitudinal dimers by the dotted lines, and the singlet configurations by the dashed lines. The dimer separation is maintained at 5 nm. Inset shows the distribution of chromophores for a transverse dimer setup. The chromophore distribution extents along the x and z directions are shown as L_x and L_z:

The two main metrics we use to analyze spasing behavior are the mean plasmon number which quantifies the strength of the spasing and the second-order coherence of the plasmon distribution, which quantifies the quality of the spasing as a measure of coherence of the plasmons created. Solving for the plasmon density matrix grants us access to the full probability distribution of plasmon excitation and, hence, the calculation of both quantities is quite straightforward. The mean plasmon number $N_{\text{pl}} = \langle \hat{a}^\dagger \hat{a} \rangle$ can be calculated using the reduced density matrix elements solutions from Eq. (32) as

$$N_{\text{pl}} = \sum_{\mu} \mu \rho_{\mu\mu}. \tag{35}$$

A higher mean plasmon number is indicative of higher intensity spasing. Similarly, the second-order coherence $g^2_{\text{pl}} = \frac{\langle \hat{a}^\dagger \hat{a}^\dagger \hat{a} \hat{a} \rangle}{\langle \hat{a}^\dagger \hat{a} \rangle^2}$ can be calculated as

$$g^2_{\text{pl}} = \frac{\sum_\mu \mu(\mu - 1)\rho_{\mu\mu}}{N^2_{\text{pl}}}. \tag{36}$$

A second-order coherence value of 1 signifies a perfectly coherent stimulated emission output while it reaches values of 2 for random noise. Hence, ideally, values closer to 1 are preferred in spasing.

We start off by comparing three spasing curves for spasers made of chromophore setups with $L_x = L_y = L_z = 50$ nm for 10-nm silver spheres in Fig. 9. The three curves are longitudinal setup with $D = 25$ nm, transverse setup with $D = 25$ nm, and a singlet setup. We also plot the second-order coherence values in the same graphs.

As we can clearly see, the singlet setup outperforms the dimer setups both in terms of quantity (mean plasmon number) and quality (second-order coherence) at almost all simulated pumping power values. We also observe that, in general, the longitudinal spasing setup has higher intensity spasing

output as compared to the transverse setup. However, in terms of second-order coherence, the transverse configuration seems to consistently have the more ideally coherent output.

Looking closer, we see that for small pumping values, the singlet performs best, followed by the transverse dimer and the longitudinal dimer, respectively. At this early stage, the spasing output seems to increase linearly with the pumping power while, more interestingly, the second-order coherence increases as well. This increase in second-order coherence is indicative of the fact that actual stimulated emission has not set in as of yet in the system and that the emission in that range corresponds only to amplified spontaneous emission. This also demonstrates that the linear increase in spasing output by itself is not a reliable indicator of spasing.

However, at a certain pumping value we observe a sudden decrease of second-order coherence for all three setups. This occurs at an electric field strength of $E_0 = 4 \times 10^4$ Vm^{-1} for the dimer setups and at $E_0 = 2 \times 10^4$ Vm^{-1} for the singlet. This decline of second-order coherence is soon followed by a visible increase in the slope of the spasing curves. This visible "kink" in the spasing curve is much less pronounced as compared to conventional lasing systems. However, this may be considered a clear sign of the threshold of spasing systems due to the simultaneous decrease in the value of the second-order coherence. A previous quantum study on the nature of spasing concluded that the spaser showed thresholdless behavior due to the lack of a clear spasing transition from spontaneous and stimulated emission [19]. This difference is due to our assumption that the 1-0 transition of the gain elements having negligible decay rates. For larger decay rates, the amplified spontaneous emission is suppressed by the chromophore decays causing less amplification along with less buildup of incoherent plasmonic population. Hence, for sufficiently low gain decay rates, spasing systems do display threshold behavior. A similar behavior of the second-order coherence was predicted for lasing in the bad cavity limit using a Fokker-Planck approach [44]. Functionally, spasing systems and bad cavity lasers are similar due to the very high plasmonic dissipations in spasing setups.

Beyond threshold, singlet curve shows the steeper gradient while the longitudinal dimer curve, lagging behind the transverse dimer curve up until this point, increases with a higher gradient than the transverse setup. Concurrently, we see the second-order coherence values of all three setups decrease rapidly to reach values close to 1 for high pump powers.

Next, we study the spasing output variation with dimer separation. Figure 10(a) displays the mean plasmon number of the spasing setups for transverse (red) and longitudinal (blue) configurations composed of 10-nm nanospheres pumped with an electric field $E_0 = 1 \times 10^5$ Vm^{-1} with a cubic gain medium distribution of size 100 nm on each side. In general, we observe that the transverse setup exhibits higher intensity spasing. As the separation is increased, the transverse dimer shows a generally increasing behavior. The longitudinal dimer, on the other hand, experiences a reduction in emissions before recovering for larger separation values. This can be understood by three key factors affecting the spasing output as separation is increased:

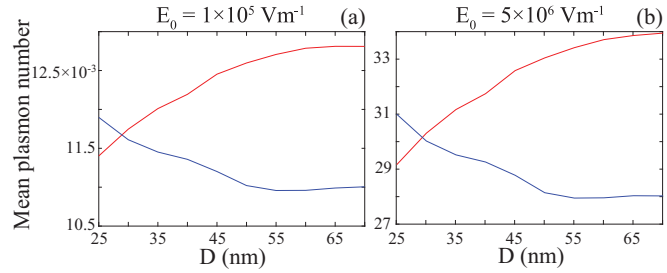

FIG. 10. Variation of the mean plasmon number with the separation between dimers for transverse (red) and longitudinal (blue) configurations. The nanosphere radius is $R = 10$ nm and the gain medium distribution has $L_x = L_y = L_z = 100$ nm.

(1) the change in radiative dissipation rate;

(2) the reduction in field confinement in the dimer hot spot (electric field leakage);

(3) the increase in the proportion of chromophores in the dimer hotspot.

For a transverse dimer, as discussed previously, interference effects and resonance frequency redshift causes the radiative dissipations to decrease with increasing dimer separation. This acts to increase spaser output. However, the increased dimer gap also allows a higher proportion of the gain medium to access the dimer hot spot and strongly couple to the plasmons generated. But, this comes with the downside of the decrease in intensity of the hot spot due to leakage. Hence, factors 2 and 3 act in opposition to each other. Figure 10 suggests that, in general, the radiative dissipation rate and the increasing chromophores within the dimer gap dominate, causing a general increase in spasing output for transverse dimers. However, for larger separations, the spaser output plateaus, showing the influence of the electric field leakage.

For longitudinal dimers, the radiative dissipation shows a peaked behavior before reducing for large separations. Similar to the transverse case, the reduction in field confinement and increase in the proportion of gain chromophores strongly coupled to the plasmons act in opposition to one another when spaser output intensity is concerned. However, as shown in Fig. 10, the longitudinal dimer output first decreases and then recovers to increase with increasing separation. The lowest spaser output almost perfectly coincides with the radiative dissipation minimum (see Fig. 8), which indicates that radiative dissipation is the dominant force determining the spasing output for smaller separations. However, for larger separations, the longitudinal setup shows a plateauing behavior similar to the transverse setup due to the reduction in electric field confinement.

We perform the same analysis for a dimer spaser setup pumped with a field $E_0 = 5 \times 10^6$ Vm^{-1} in Fig. 10(b) [a field 2500-fold more intense as compared to that of Fig. 10(a)]. We again clearly see a similar pattern of behavior for transverse and longitudinal configurations.

Finally, we present the variation of the spaser output with the size of the gain medium. Figure 11 displays the variation of the spaser emission intensity and second-order coherence value for the two dimer configurations as well as the singlet configuration with the length of a cubic gain medium. The

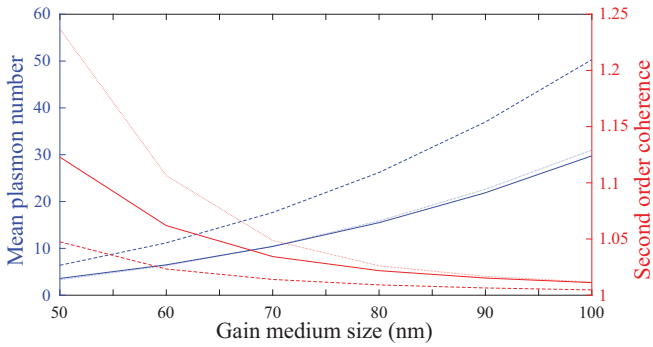

FIG. 11. The variation of the mean plasmon number (blue) and second-order coherence (red) for transverse dimer (solid line), longitudinal dimer (dotted line), and singlet (dashed line) setups with the size of the surrounding cubic gain medium. The shown size indicates the length of one side of the gain medium cube. The nanospheres are of 10-nm radius and the separation $D = 5$ nm for the dimer setups. The pump field is held constant at $E_0 = 5 \times 10^6$ Vm^{-1}.

displayed size is the length of one side of the cube. We observe the dramatic increase in the spasing output intensity as well as the decrease of the second-order coherence value to 1. It has been observed in other studies done on spasing in three-level gain media that the spasing output tends to follow a linear variation with the number of gain chromophores given that the gain chromophores are identical [18]. In our case, we observe that the spasing output displays a subcubic dependence on the gain medium length. This is due to the fact that while the number of chromophores grows as the cube of the length, the chromophores are not identical and the couplings of chromophores from further away is much weaker compared to the ones closer to the plasmon.

We also note that for smaller gain medium distributions the transverse dimer spaser output is higher than that of the longitudinal. But, as the size of the gain medium and the number of chromophores increase, the longitudinal dimer overtakes the transverse.

IV. CONCLUSION

In this paper, we have developed the complete cavity quantum electrodynamic model of a nanosphere dimer spaser operating in the bright plasmonic modes. We perform canonical quantization of the two main dimer configurations and deduce the couplings of the system with gain media chromophores. We also calculate the blueshifted and redshifted resonance frequencies of the dimer setups as compared to the singlet setup within the dipole approximation.

We analytically calculate the radiative dissipations in dimer setups, showing interesting characteristics under varying dimer separations, with effects governed by the resonance frequency shift and the interference between the two dimer radiation patterns.

As expected through the results of semiclassical analyses done previously, longitudinal dimers display better field confinement and hence better spasing characteristics in general as compared to transverse dimers. Our results confirm that for small dimer gap, large pumping power, and large gain media chromophore numbers, longitudinal dimers do perform better than transverse dimers under the same conditions. However, transverse dimers outperform longitudinal dimers significantly at lower pump power values, larger dimer separations, and smaller number of gain media chromophores.

We also find that, while the longitudinal configuration does indeed show optimal spasing at the smallest separation we study, remarkably, transverse dimers show increasing spasing output as dimer separation is increased. So, we discover that, despite its weak field confinement, the transverse dimer actually performs much better than the longitudinal dimer in applications when restrictions are imposed on pump power, dimer separation, and chromophore number. We also show that in all circumstances, transverse dimer setups produce higher coherent spasing output when compared to longitudinal dimers under the same conditions.

These results suggest that in biological environments, or other restrictive environments, where pump power needs to be weak while there is no avenue to increase the gain medium extent or the concentration of the chromophores, transverse dimers may actually be the most suitable option. These observations also suggest that to achieve maximal spasing in coupled nanosphere based structures, the spacing between spheres along the direction of the external field should be minimal while the spacing in the directions perpendicular should have an optimal spacing as prescribed by the radiation profile.

We also find that, for quantum spasing systems, a visible threshold in the spasing curve does not exist in general. This has been observed in other studies [19]. However, we do observe a sudden increase in the coherence of the spasing output, which signals the onset of stimulated emission for the parameter ranges we use. We also observe a subsequent minor increase in the gradient of the spasing curve, which also signifies the onset of spasing. This observation has not been reported for quantum spasing systems.

We finally note that while the method we present is focused on dimers, the same methodology can be used to analyze more complex setups of interacting nanospheres such as trimer, tetramer, or even more esoteric setups. We do, however, need to emphasize that our use of the dipole approximation will not hold true for extremely large or small separations of spheres, due to far-field effects in the first instance, and due to higher-order multipole effects in the second. The single-mode analysis we have presented of the spaser also needs to be modified for dimer setups with extremely small gaps, due to the overlap of higher-order modes with the dipole bright spasing mode. Dark modes may also be incorporated by considering differently polarized incident light fields.

[1] M. Premaratne and M. I. Stockman, Theory and technology of spasers, Adv. Opt. Photonics **9**, 79 (2017).

[2] Y. E. Lozovik, I. A. Nechepurenko, A. V. Dorofeenko, E. S. Andrianov, and A. A. Pukhov, Spaser spectroscopy with subwavelength spatial resolution, Phys. Lett. A **378**, 723 (2014).

[3] E. I. Galanzha, R. Weingold, D. A. Nedosekin, M. Sarimollaoglu, J. Nolan, W. Harrington, A. S. Kuchyanov,

R. G. Parkhomenko, F. Watanabe, Z. Nima *et al.*, Spaser as a biological probe, Nat. Commun. **8**, 15528 (2017).

[4] C. Rupasinghe, W. Zhu, and M. Premaratne, Spaser powered photothermal cancer therapy using graphene and carbon nanotubes, in *2014 IEEE Photonics Conference* (IEEE, Piscataway, NJ, 2014), pp. 16–17.

[5] D. J. Bergman and M. I. Stockman, Surface Plasmon Amplification by Stimulated Emission of Radiation: Quantum Generation of Coherent Surface Plasmons in Nanosystems, Phys. Rev. Lett. **90**, 027402 (2003).

[6] M. Noginov, G. Zhu, A. Belgrave, R. Bakker, V. Shalaev, E. Narimanov, S. Stout, E. Herz, T. Suteewong, and U. Wiesner, Demonstration of a spaser-based nanolaser, Nature (London) **460**, 1110 (2009).

[7] B. Liu, W. Zhu, S. D. Gunapala, M. I. Stockman, and M. Premaratne, Open resonator electric spaser, ACS Nano **11**, 12573 (2017).

[8] L. Kumarapperuma, M. Premaratne, P. K. Jha, M. I. Stockman, and G. P. Agrawal, Complete characterization of the spasing (ll) curve of a three-level quantum coherence enhanced spaser for design optimization, Appl. Phys. Lett. **112**, 201108 (2018).

[9] J. B. Khurgin and G. Sun, Comparative analysis of spasers, vertical-cavity surface-emitting lasers and surface-plasmon-emitting diodes, Nat. Photonics **8**, 468 (2014).

[10] S. Biswas, J. Duan, D. Nepal, R. Pachter, and R. Vaia, Plasmonic resonances in self-assembled reduced symmetry gold nanorod structures, Nano Lett. **13**, 2220 (2013).

[11] A. Yang, T. B. Hoang, M. Dridi, C. Deeb, M. H. Mikkelsen, G. C. Schatz, and T. W. Odom, Real-time tunable lasing from plasmonic nanocavity arrays, Nat. Commun. **6**, 6939 (2015).

[12] S. Zou, N. Janel, and G. C. Schatz, Silver nanoparticle array structures that produce remarkably narrow plasmon lineshapes, J. Chem. Phys. **120**, 10871 (2004).

[13] A. Salmanogli and H. S. Gecim, Array of nanoparticles coupling with quantum-dot: Lattice plasmon quantum features, Phys. E (Amsterdam) **100**, 54 (2018).

[14] K. Li, X. Li, M. I. Stockman, and D. J. Bergman, Surface plasmon amplification by stimulated emission in nanolenses, Phys. Rev. B **71**, 115409 (2005).

[15] E. S. Andrianov, A. A. Pukhov, A. V. Dorofeenko, A. P. Vinogradov, and A. A. Lisyansky, Stationary behavior of a chain of interacting spasers, Phys. Rev. B **85**, 165419 (2012).

[16] E. Prodan, C. Radloff, N. J. Halas, and P. Nordlander, A hybridization model for the plasmon response of complex nanostructures, Science **302**, 419 (2003).

[17] T. Warnakula, M. I. Stockman, and M. Premaratne, Improved scheme for modeling a spaser made of identical gain elements, JOSA B **35**, 1397 (2018)

[18] Y. Zhang and K. Mølmer, Amplified emission and lasing in a plasmonic nanolaser with many three-level molecules, Phys. Rev. A **97**, 013837 (2018).

[19] M. Richter, M. Gegg, T. S. Theuerholz, and A. Knorr, Numerically exact solution of the many emitter–cavity laser problem: Application to the fully quantized spaser emission, Phys. Rev. B **91**, 035306 (2015).

[20] Y. Zhang and V. May, Theory of molecule metal nano-particle interaction: Quantum description of plasmonic lasing, J. Chem. Phys. **142**, 224702 (2015).

[21] S. Franke, S. Hughes, M. K. Dezfouli, P. T. Kristensen, K. Busch, A. Knorr, and M. Richter, Quantization of Quasinormal Modes for Open Cavities and Plasmonic Cavity Quantum Electrodynamics, Phys. Rev. Lett. **122**, 213901 (2019).

[22] P. Y. Chen, D. J. Bergman, and Y. Sivan, Generalizing Normal Mode Expansion of Electromagnetic Green's Tensor to Open Systems, Phys. Rev. Appl. **11**, 044018 (2019).

[23] Y. Jiang, S. Pillai, and M. A. Green, Realistic silver optical constants for plasmonics, Sci. Rep. **6**, 30605 (2016).

[24] P. B. Johnson and R.-W. Christy, Optical constants of the noble metals, Phys. Rev. B **6**, 4370 (1972).

[25] G. Mie, Beiträge zur optik trüber medien, speziell kolloidaler metallösungen, Ann. Phys. **330**, 377 (1908).

[26] I. D. Mayergoyz, D. R. Fredkin, and Z. Zhang, Electrostatic (plasmon) resonances in nanoparticles, Phys. Rev. B **72**, 155412 (2005).

[27] M. I. Stockman, Nanoplasmonics: Past, present, and glimpse into future, Opt. Express **19**, 22029 (2011).

[28] J. D. Jackson, *Classical Electrodynamics* (Wiley, New York, 1975).

[29] E. Waks and D. Sridharan, Cavity qed treatment of interactions between a metal nanoparticle and a dipole emitter, Phys. Rev. A **82**, 043845 (2010).

[30] L. D. Landau, J. Bell, M. Kearsley, L. Pitaevskii, E. Lifshitz, and J. Sykes, *Electrodynamics of Continuous Media*, Vol. 8 (Elsevier, Amsterdam, 2013).

[31] J. B. Khurgin, How to deal with the loss in plasmonics and metamaterials, Nat. Nanotechnol. **10**, 2 (2015).

[32] M. O. Scully and M. S. Zubairy, *Quantum Optics* (Cambridge University Press, Cambridge, 1997).

[33] P. Drude, Zur elektronentheorie der metalle, Ann. Phys. **306**, 566 (1900).

[34] R. H. Dicke, Coherence in spontaneous radiation processes, Phys. Rev. **93**, 99 (1954).

[35] H. Carmichael, *An Open Systems Approach to Quantum Optics: Lectures Presented at the Université Libre de Bruxelles, October 28 to November 4, 1991*, Vol. 18 (Springer, Berlin, 2009).

[36] V. A. Markel, Introduction to the maxwell garnett approximation: tutorial, J. Opt. Soc. Am. A **33**, 1244 (2016).

[37] C. F. Bohren and D. R. Huffman, *Absorption and Scattering of Light by Small Particles* (Wiley, Hoboken, NJ, 2008).

[38] T. J. Davis, K. C. Vernon, and D. E. Gómez, Designing plasmonic systems using optical coupling between nanoparticles, Phys. Rev. B **79**, 155423 (2009).

[39] K. Madoyan, A. Melikyan, and H. Minassian, Radiation damping of surface plasmons in a pair of nanoparticles and in nanoparticles near interfaces, J. Phys. Chem. C **116**, 16800 (2012).

[40] C. Dahmen, B. Schmidt, and G. von Plessen, Radiation damping in metal nanoparticle pairs, Nano Lett. **7**, 318 (2007).

[41] D. Marinica, A. Kazansky, P. Nordlander, J. Aizpurua, and A. G. Borisov, Quantum plasmonics: Nonlinear effects in the field enhancement of a plasmonic nanoparticle dimer, Nano Lett. **12**, 1333 (2012).

[42] P. Nordlander, C. Oubre, E. Prodan, K. Li, and M. Stockman, Plasmon hybridization in nanoparticle dimers, Nano Lett. **4**, 899 (2004).

[43] J. R. de Lasson, J. Mørk, and P. T. Kristensen, Three-dimensional integral equation approach to light scattering, extinction cross sections, local density of states, and quasi-normal modes, J. Opt. Soc. Am. B **30**, 1996 (2013).

[44] S. Gnutzmann, Photon statistics of a bad-cavity laser near threshold, Eur. Phys. J. D **4**, 109 (1998).